Bull Math Biol (2012) 74:474–490
DOI 10.1007/s11538-011-9703-z

ORIGINAL ARTICLE

Spatial Analysis of Multi-species Exclusion Processes: Application to Neural Crest Cell Migration in the Embryonic Gut

Benjamin J. Binder · Kerry A. Landman · Donald F. Newgreen · Johanna E. Simkin · Yoshiko Takahashi · Dongcheng Zhang

Received: 5 July 2011 / Accepted: 21 October 2011 / Published online: 24 November 2011

Abstract Hindbrain (vagal) neural crest cells become relatively uniformly distributed along the embryonic intestine during the rostral to caudal colonization wave which forms the enteric nervous system (ENS). When vagal neural crest cells are labeled before migration in avian embryos by in ovo electroporation, the distribution of labeled neural crest cells in the ENS varies vastly. In some cases, the labeled neural crest cells appear evenly distributed and interspersed with unlabeled neural crest cells along the entire intestine. However, in most specimens, labeled cells occur in relatively discrete patches of varying position, area, and cell number. To determine reasons for these differences, we use a discrete cellular automata (CA) model incorporating the underlying cellular processes of neural crest cell movement and proliferation on a growing domain, representing the elongation of the intestine during development. We use multi-species CA agents corresponding to labeled and unlabeled neural crest cells. The spatial distributions of the CA agents are quantified in terms of an index. This investigation suggests that (i) the percentage of the initial neural crest cell population that is labeled and (ii) the ratio of cell proliferation to motility

B.J. Binder (✉)
School of Mathematical Sciences, University of Adelaide, Adelaide, South Australia 5005, Australia
e-mail: benjamin.binder@adelaide.edu.au

K.A. Landman
Department of Mathematics and Statistics, University of Melbourne, Parkville, Victoria 3010, Australia

D.F. Newgreen · J.E. Simkin · D. Zhang
Embryology Research Group, Murdoch Childrens Research Institute, Parkville, Victoria 3052, Australia

Y. Takahashi
Graduate School of Biological Sciences, Nara Institute of Science and Technology, Nara 630-0101, Japan

are the two key parameters producing the extreme differences in spatial distributions observed in avian embryos.

Keywords Neural crest cells · In ovo electroporation · Cellular automata model · Spatial-point data sets

1 Introduction

Advances in cell labeling and imaging techniques are providing biologists with a wealth of information. Cell labeling allows for the detection of specific cell types in situations where they would otherwise be invisible or indistinguishable from neighboring cell types. However, in some instances the labeling is not taken up by the whole of the intended population of cells. Therefore, only a sub-population of cells within a larger population of unlabeled (and undetected) cells of the same type occurs. The result at the end of a developmental process of this initial incomplete labeling can be complicated and interpretation may not be obvious. Here, we investigate such a case: the spatial distribution of labeled neural crest-derived cells in the enteric nervous system (ENS) by analyzing spatial-point data sets generated from discrete mathematical models.

Gut activities such as peristalsis are controlled by the ENS, a large and complex neural network in the wall of the gastrointestinal tract. A relatively small number of cells, originating from the hindbrain (or vagal) neural tube, enter the foregut rostrally and colonize the whole gastrointestinal tract as a rostro-caudally (oro-anally) directed and timetabled wave advancing within the gut mesoderm (Allan and Newgreen 1980). These enteric neural crest (ENC) cells eventually differentiate as ENS neurons and glial cells that coalesce into the ganglionated network typical of the mature ENS (Hao et al. 2009). A relatively common birth defect, called Hirschsprung's disease, results when this migratory wave fails to reach the anal end—this segment of gut therefore lacks an ENS and cannot generate peristaltic contractions. The complications from intractable constipation that results can be fatal if not treated by surgical removal of the affected region (Newgreen and Young 2002). Stem cell treatment of Hirschsprung's disease has the potential to revolutionize current treatments. However, full exploitation of such methodology is likely to benefit from an understanding of the biological "rules" of normal ENC colonization and ENS formation.

Along with the migratory ability of ENC cells, there must be a large expansion of ENC cell numbers by cell division (Young et al. 2005) for complete colonization. The ENC cell number and density increases, through proliferation, to reach a preferred density appropriate for each segment of intestinal mesenchyme, which forms the gut wall. Simultaneously, the mesenchymal cells which make up the gut tissue are dividing rapidly leading to gut growth (Binder et al. 2008), which impacts upon gut colonization by ENC cells (Newgreen et al. 1996). The principle axis of growth is longitudinal, by mesenchymal cell division throughout the gut tissue resulting in elongation (Binder et al. 2008; Newgreen et al. 1996).

The labeling of cells before migration is a technique for interrogating complex colonization processes (Bhattacharyya et al. 2008). We use this technique here, and the

detailed experimental methods are presented in Appendix. Using Green Fluorescent Protein (GFP) gene constructs that integrate into the genome (Sato et al. 2007), avian ENC cells can be permanently labeled with GFP by electroporation in ovo while in the neural tube, before making their way to the developing intestine (Fig. 1(a)). When a GFP-labeled ENC divides, its two daughters inherit the GFP gene and are also labeled with this protein. With conventional non-integrating GFP constructs, cell division results in gene dosage dilution. This means that in the highly proliferative ENS, effective GFP expression is soon lost except in those cells that rapidly differentiate as post-mitotic ENS neurons. However, with in ovo electroporation, the gene construct does not transfect all available cells. Only a percentage of ENC cells are labeled with GFP, and this percentage is not known precisely. After successful colonization of the intestine, staining of the gut tissue showed a distribution of GFP-labeled ENC cells amongst unlabeled (and, therefore, undetected) ENC cells. These unlabeled cells were revealed later by immuno-labeling for ENC markers. Images taken from quail gut showed a surprising amount of variability between the spatial distributions of labeled ENC cells in different embryos. In some specimens (Fig. 1(b)), the GFP-labeled cells occurred throughout the whole gut to the ENC wavefront, although the density of labeled cells was not entirely uniform. In more frequent specimens (Figs. 1(c) and (d)), there were distinct and separate patches of labeled cells, with intervening regions devoid of labeled ENC cells. In both cases, unlabeled ENC cells were always distributed throughout the gut (Figs. 1(e) and (f)).

To gain a better understanding of the basis for variability of these ENC cell spatial distributions (labeled and unlabeled), we use a cellular automata (CA) model to investigate the effect of four key mechanisms in the developing ENC cell migration process (Binder et al. 2008; Binder and Landman 2009; Simpson et al. 2007a, 2007b; Zhang et al. 2010). The mechanisms comprise of ENC cell motility, ENC cell proliferation, the initial number or density of ENC cells that are labeled at the start of the migration and the underlying gut tissue growth. We find that the variation in the ENC cell spatial distribution is due mainly to the initial proportion of labeled ENC cells and the ratio of ENC cell proliferation rate to ENC cell motility.

2 The Model and Index

In the developing gut, ENC cells invade the thick intestinal wall, which is a mesenchymal cell mass, but are restricted to a relatively narrow layer, as on the surface of a cylinder. Following Binder et al. (2008), Binder and Landman (2009), we use a two-dimensional CA model (with unit square lattice spacing) to simulate the ENC cell migration. We have two types of CA agents, domain and ENC, each with unit area.

Domain agents represent the underlying growing intestinal tissue cells. The domain is assumed to increase in length (in the x-direction) with time t, given by $L(t)$. The circumference Y is fixed, as the radial expansion of gut tissue is relatively small compared to elongation in length (Binder et al. 2008; Newgreen et al. 1996). The domain consists of sites within a rectangular lattice $(L(t), Y)$ whose positions are located at the discrete integer points (x, y), where $1 \leq x \leq L(t)$ and $1 \leq y \leq Y$. Each

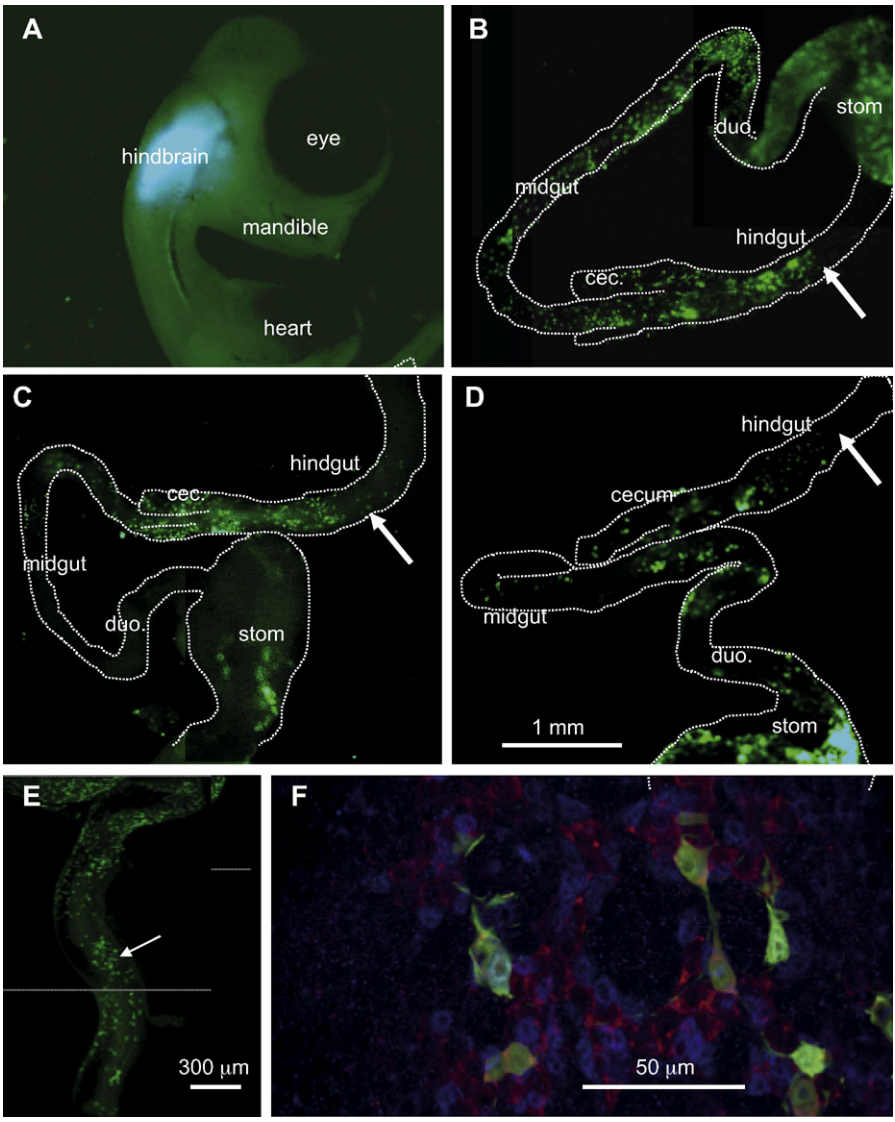

Fig. 1 Quail embryo gut experimental results. Here, the labeled ENC cells are green. (**A**) At embryonic age 6.5 days (E6.5), quail embryo electroporated at E1.5 in the hindbrain shows GFP expression persisting in this region. (**A**–**E**) Gastrointestinal tracts removed from similar embryos have GFP expression in ENC cell immigrants, in widely variable patterns. Examples: (**B**) GFP+ve ENC may occur relatively densely at all regions of the gastrointestinal tract, (**C**) densely in some regions, here in distal midgut, cecum, and hindgut or (**D**) in widely separate patches. The position of the ENC wavefront is indicated by *the arrow* in (**B**–**D**). Even where the GFP+ve cells are dense, for example (**E**) in the midgut (indicated by *the arrow*), (**F**) immuno-labeling and confocal microscopy reveals there are many more unlabeled ENC cells (*blue* nuclei, anti-SoxE) and ENC-derived neurons (*red* cytoplasm, anti-HuC/D) in the same region. Gut regions in rostro-caudal order are: stomach (stom), duodenum (duo), midgut (small intestine), cecum, and hindgut (large intestine)

of the lattice sites is occupied by a single domain agent. During a single time step from t to $t+1$ of the algorithm, for each row in the lattice, a pre-determined number of domain agents $n(t)$ are randomly selected to proliferate by mitotic division. Here, $n(t)$ is the nearest integer value or "round" of $L(t+1) - L(t)$. If a domain agent at (x, y) proliferates, the original domain agent moves to $(x+1, y)$, and a new domain agent is inserted at (x, y). All domain agents to the right of (x, y) also move one unit in the positive x-direction. This growth mechanism is stochastic as domain agents are randomly selected to proliferate, but the overall length of each row in the domain $L(t)$ is the same at time t.

ENC agents undergo motility and proliferation mechanisms with exclusion. Only one ENC agent is permitted to occupy any one of the lattice sites at any time. Therefore, each site is either occupied by a single domain agent or by a single domain agent together with a single ENC agent. If an ENC agent is occupying the same site as a domain agent that moves to a new position in the lattice due to domain agent proliferation, then the ENC agent is transported or carried to this new position in the lattice.

The ENC agents move and proliferate independently of the growing domain by the mechanisms outlined below. The domain contains $m(t)$ ENC agents at time t. During a single time step from t to $t+1$, first $m(t)$ ENC agents are selected randomly and given the opportunity to move, and then $m(t)$ ENC agents are selected randomly and given the opportunity to proliferate. A ENC agent at (x, y) that is chosen to move attempts to move with probability P_m $(0 \leq P_m \leq 1)$ to one of the four nearest neighbors $(x \pm 1, y \pm 1)$ each with probability $1/4$. When considering a potential proliferation event, a mother ENC agent attempts to divide with probability P_p $(0 \leq P_p \leq 1)$, and one daughter replaces the parent and the second daughter agent is deposited into one the nearest neighbor sites $(x \pm 1, y \pm 1)$ with probability $1/4$. We choose boundary conditions appropriate for the surface of a finite length cylinder. Periodic boundary conditions are imposed on $y = 0$ and $y = Y$ (so that an agent located at $(x, 0)$ appears at (x, Y) after moving in the negative y direction, and an agent located at (x, Y) appears at $(x, 0)$ after moving in the positive y direction), and ENC agents at $x = 0$ and $x = L$ are not permitted to move in the negative and positive directions, respectively. If the target site is occupied for any motility or proliferation event, then that event is aborted (as in an exclusion process).

We define $c_i(x, t)$ to be the total number of ENC agents in column x of the lattice after t steps of the ith realization. Then for N realizations starting from the same initial condition, we can define an average column agent density as

$$C(x, t) = \frac{1}{NY} \sum_{i=1}^{N} c_i(x, t). \tag{1}$$

Binder et al. (2009) showed that the average column density of motile proliferative agents on a growing domain, represented by $C(x, t)$, is given by the solution to a partial differential equation:

$$\frac{\partial C}{\partial t} = \frac{P_m}{4} \frac{\partial^2 C}{\partial x^2} + P_p C(1 - C) + \frac{\partial^2 (D_L C)}{\partial x^2} - \frac{\partial (vC)}{\partial x}, \tag{2}$$

where

$$v(x,t) = \frac{\mathrm{d}L}{\mathrm{d}t}\frac{x}{L(t)}, \qquad D_L(x,t) = \frac{\mathrm{d}L}{\mathrm{d}t}\frac{L(t)}{2(L(t)+1)}\frac{x}{L(t)}\left(1-\frac{x}{L(t)}\right), \tag{3}$$

provided $P_p/P_m \ll 1$. The terms on the right-hand side of (2) correspond to (i) diffusive properties of the ENC motility mechanism, (ii) a logistic term due to ENC agent proliferation (Simpson et al. 2010), (iii) local diffusive/dispersive properties of the domain agent growth mechanism, and (iv) advection due to the domain agent growth mechanism. Later, (2)–(3) will be useful when analyzing and discussing the CA modeling results (for the total ENC agent population).

To simulate the GFP-labeled ENC cell migration observed in the experiments (Fig. 1), we introduce two species of ENC agents. These species are identical with respect to motility and proliferation ability, and differ only in that one species is red (representing GFP-labeled ENC cells) and the other green (representing un-labeled ENC cells). When an ENC agent undergoes a proliferation event, the color of the parent agent (red or green) is inherited by the two daughters. Each simulation of the model produces a spatial distribution of the two species of ENC agents.

We quantify the spatial distribution of the two species (and total ENC agent population) by adapting and calculating indices developed by Binder and Landman (2011). When compared with their corresponding limiting values, they are indicative of a spatial distribution's deviation from an evenly distributed state.

Therefore, at any time t, we consider our $L(t) \times Y$ rectangular domain which is populated with a total of $n(t)$ ENC agents. The domain is divided into $M(t)$ equal-sized bins. Even though these bins are equal in size at any given time, they need not necessarily be the same size for all time. If $b_j(t)$ is the number of ENC agents in bin j, $(j = 1, \ldots, M(t))$, then the average bin count is n/M and the population variance is

$$\sigma(t)^2 = \frac{1}{M}\sum_{j=1}^{M}\left(b_j - \frac{n}{M}\right)^2. \tag{4}$$

The index is a scaled variance given by

$$I(t) = \frac{\sigma^2}{\sigma_0^2}, \tag{5}$$

where

$$\sigma_0(t)^2 = n^2\left(\frac{M-1}{M^2}\right). \tag{6}$$

For a single realization, the index can undergo large fluctuations, but these can be decreased by summing over N realizations and defining the average index as

$$\bar{I}(t) = \frac{1}{N}\sum_{i=1}^{N} I_i, \tag{7}$$

where I_i is the ith realization of the index. The index (and its average) lies in [0, 1], where $I = \bar{I} = 0$ corresponds to an even distribution and $I = \bar{I} = 1$ to maximum segregation.

However, an even distribution is an idealized state that is not often realized. Instead, the more realistic scenario occurs when each ENC agent is equally likely to lie in any bin. Such a state is termed *complete spatial randomness* (CSR) (Diggle 1983; Jones 1991; Phelps and Tucker 2006), and once the CSR state is achieved the distribution of ENC agents cannot be made any more even. The CSR limit for the index is

$$I_{x\mathrm{csr}}(t) \approx \frac{1-d}{n}, \tag{8}$$

where

$$d(t) = \frac{n}{LY} \tag{9}$$

is the average ENC agent density.

We compute the average indices for the two species of ENC agents and total population of ENC agents, comparing them to each other and their corresponding CSR values. In the calculations that follow, the bins have the same constant area (greater than unity) for all time. For a growing domain the number of bins $M(t)$ increases with time, and $L(t)Y$ is divisible by $M(t)$ with remainder zero.

3 Results

The spatial distribution resulting from motility, proliferation, and growing domain processes is examined for two species of ENC agents. In the following results, we consider in turn each mechanism separately, and then allow multiple mechanisms to act simultaneously. Although we make no attempt here to parameterize our CA model with physical quantities associated with the experiments (e.g. cell proliferation and motility rates, tissue length and cell sizes), we find qualitatively similar results for a wide range of parameter values. This provides a qualitative understanding of the nature of the ENC cell spatial distributions observed in the experiments.

In all the simulations, we initially ($t = 0$) populate the domain with two species of ENC agents, by randomly selecting unoccupied lattice sites. We denote the densities of the two species by d_r and d_g, and the total population as $d = d_r + d_g$. Before analyzing the spatial data from the CA model, we use the initial condition to check the calculation of the three indices (two species and total population). We expect the spatial distributions to be at the CSR state.

Shown in Fig. 2(a) is a typical initial condition with two species (red and green) of ENC agents. The corresponding total population of ENC agents (blue) can be seen in Fig. 2(b). For any single realization of the initial condition, there are considerable fluctuations in the calculated values of the indices (red, green, blue curves) from the CSR limit (broken black curve) (Fig. 2(c)). These fluctuations are reduced when calculating average indices (Fig. 2(d)), confirming that we are calculating the indices accurately.

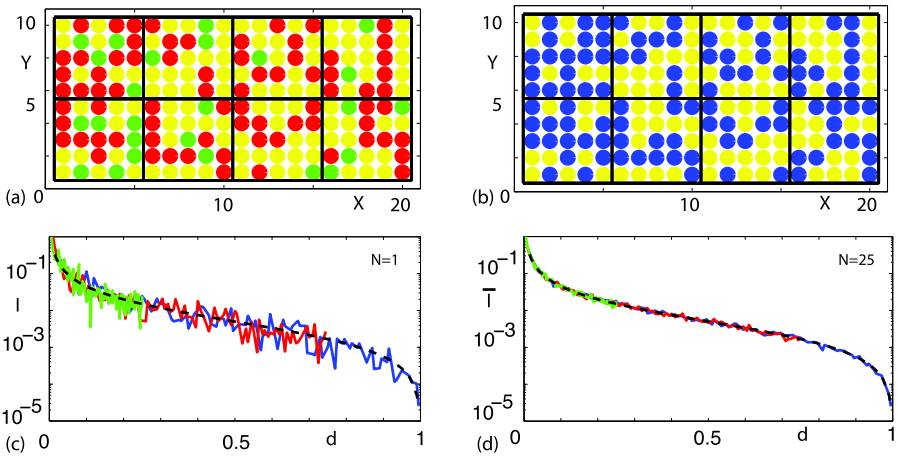

Fig. 2 Initial condition for multi-species exclusion model on a 20×10 lattice ($L = 20$ and $Y = 10$) with $M = 8$ bins. The proportion of *red* to *green* agents is 3 : 1. (**a**) Single realization with *red* and *green* agent densities $d_r = 0.375$ and $d_g = 0.125$. (**b**) Combined *red* and *green* agent population (*blue*) with density $d = d_r + d_g = 0.5$, for the realization shown in (**a**). (**c**) Calculated values of the Index I (from single realizations) for each species (*red* and *green*) and total population (*blue*) versus density d. The *broken curve* is the $I_{x\text{csr}}$ values. (**d**) Average index $\bar{I}$ (from $N = 25$ simulations) versus d. The *broken curve* is the $I_{x\text{csr}}$ values

3.1 A Single Mechanism

The motility mechanism on its own is considered next. Previous results for a single species of ENC agents showed that placement in a localized configuration spreads with time by a diffusive process (see (2)—diffusive term), and over long time attains a CSR state (Binder and Landman 2011). We know from Fig. 2 that if two species of ENC agents are placed randomly on the lattice they are each at the CSR limit. We would then expect each species to remain at the CSR limit if the agents are now allowed to move to nearest neighbor unoccupied sites. Indeed, this is confirmed in Fig. 3. The different magnitudes of the CSR limits for each species is due to the relative number of the two species—the CSR limit is highest for the species with the lowest number of ENC agents (red).

We now consider the ENC agent proliferation mechanism on its own. After randomly placing agents on the lattice (giving the CSR limit initially), the agents are allowed to proliferate by adding an ENC agent in one of the nearest neighbor unoccupied sites. Clusters or patches of the same ENC agent species are expected from this mechanism, since daughter ENC agents are unable to move after being created. Figures 4(b–c) demonstrate the evolution of the aggregation at two times ($t = 10, 100$). As time evolves, the individual species move away from their CSR limit and reach a plateau, corresponding to when all lattice sites are occupied ($d = 1$ is the carrying capacity here) (Fig. 4(d)). The behavior of the total population is different. At first, it also deviates from the CSR limit, but when the lattice approaches carrying capacity, the CSR limit is again attained (Fig. 4(d)). The proliferation mechanism transforms an (initially) evenly distributed state of agents to a more segregated state—for each

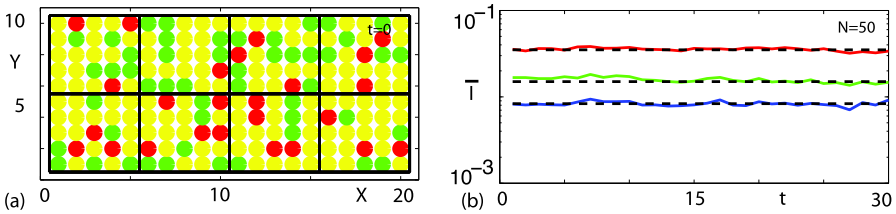

Fig. 3 Motility mechanism, with probability of motility $P_m = 1$. (**a**) Typical initial condition, the *red* and *green* agent densities are $d_r = 0.125$ and $d_g = 0.25$. (**b**) Evolution of the average index (from $N = 50$ simulations) for the two species (*red* and *green*) and total population (*blue*). The *broken black curves* are the corresponding I_{xcsr} values

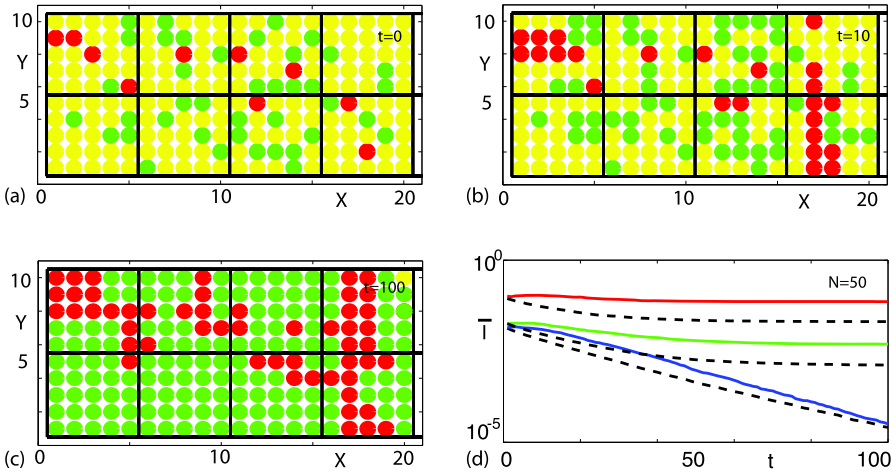

Fig. 4 Proliferation mechanism, with probability of proliferation $P_p = 0.1$. (**a**) Typical initial condition, the initial *red* and *green* agent densities are $d_r(0) = 0.05$ and $d_g(0) = 0.2$. (**b**) and (**c**) Single realizations at times $t = 10$ and $t = 100$. (**d**) Evolution of the average index (from $N = 50$ simulations) for the two species (*red* and *green*) and total population (*blue*). The *broken curves* are the corresponding I_{xcsr} values

species the segregated state remains for all time, while the total population eventually returns to the CSR state.

When considering domain growth on its own we allow the domain to elongate according to the growth mechanism, after randomly placing passive ENC agents on the lattice. In Fig. 5, we demonstrate results for linear growth

$$L(t) = L(0) + \beta t. \tag{10}$$

The densities of each species and whole population dilute with time (see (2)—advection term), since the number of ENC agents remains constant whereas the size of the domain increases with time. Hence, the CSR limits asymptote to the value $1/n$ as $t \to \infty$ (for each species and whole population, Fig. 5(c)). However, the spatial distributions remain at the CSR limit throughout this process, due to the stochastic nature of the domain growth mechanism (see (2)—local diffusive term).

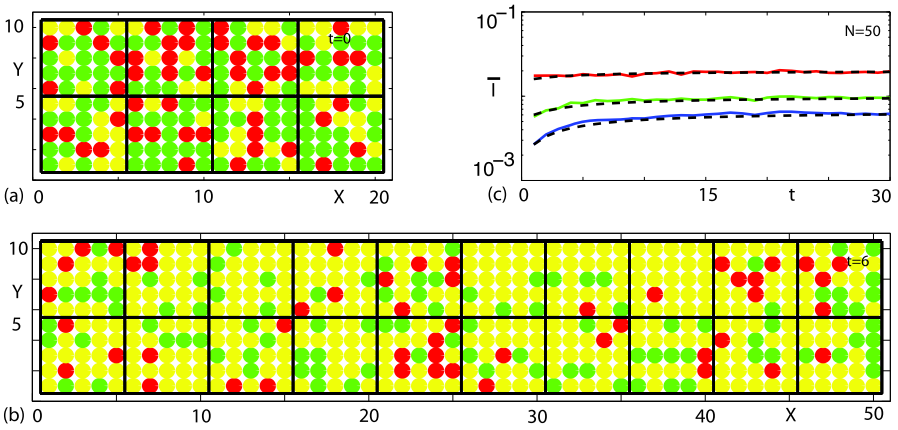

Fig. 5 Domain growth (linear) mechanism with $L(0) = 20$ and $\beta = 5$. (**a**) Typical initial condition, the *red* and *green* agent densities are $d_r(0) = 0.25$ and $d_g(0) = 0.5$. (**b**) A single realization at time $t = 6$. (**c**) Evolution of the average index (from $N = 50$ simulations) for the two species (*red* and *green*) and total population (*blue*). The *broken curves* are the corresponding I_{xcsr} values

3.2 Two Mechanisms

So far, we have seen that an initially even spatial distribution of ENC agents is unaffected by the ENC agent motility and domain agent growth mechanisms, but the ENC agent proliferation mechanism causes segregation. Next, we investigate the effect of combining two mechanisms on an initially even distribution of ENC agents. Since both the motility and domain growth mechanism kept the ENC agents spatial distributions at their CSR states, having the two operate together would be expected to give the same result. Indeed it does, and these results are not shown here.

Let us instead consider ENC agent motility and proliferation. Starting with the same initial condition as demonstrated in Fig. 4(a), we investigate two values of the proliferation rate—the first row in Fig. 6 has a moderate value $P_p = 0.1$, while the second and third row has a small value $P_p = 0.01$. The resulting spatial distributions at $t = 60$ are very different (Figs. 6(a) and (c)), and this is reflected in the values of the index (Figs. 6(b) and (d)). The higher value of the proliferation generates aggregates, and the indices of the individual species are far from the CSR state (Fig. 6(b)), just as they were for the proliferation mechanism on its own (Fig. 4(d)). For a sufficiently small proliferation rate and moderate times, the distributions of all species stay at CSR levels throughout the process. The important parameter here is the ratio of the ENC agent proliferation rate to the ENC agent motility rate, namely P_p/P_m, as expected from previous analysis (Binder and Landman 2009).

For a small proliferation rate, we further examine the long-time behavior of the indices, as shown in Fig. 6(f). Given long enough, the domain becomes fully occupied, and the individual species indices and limits asymptote to constant values in a qualitatively similar way to those with a moderate proliferation rate (see Fig. 6(b)). The indices are slightly above their corresponding CSR values for t large (red and green Fig. 6(f)), but this deviation is much smaller when compared with the results

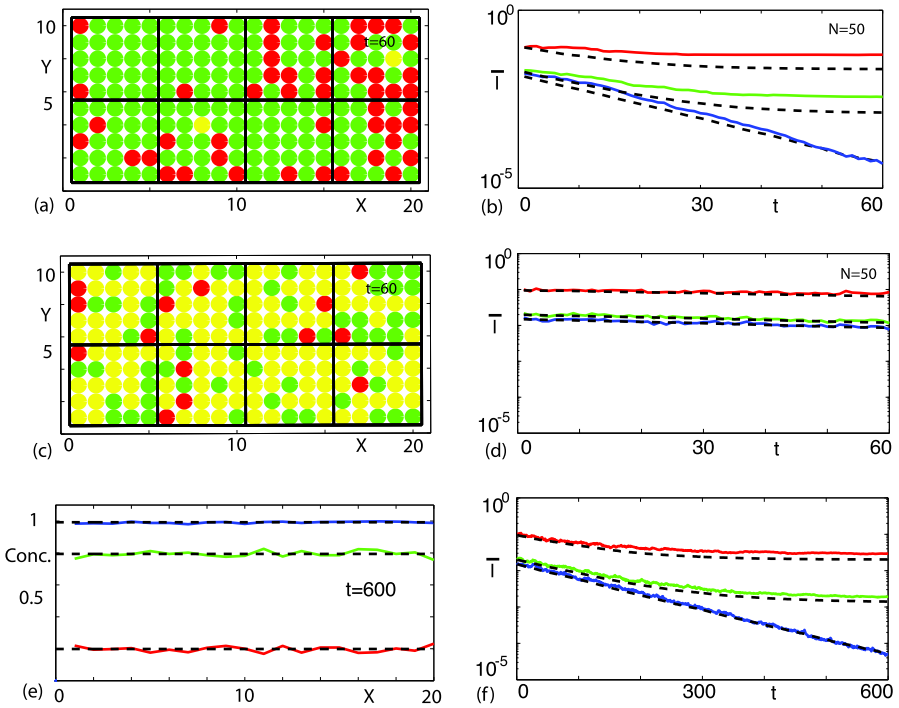

Fig. 6 Motility and proliferation mechanism, with $P_m = 1$. The initial *red* and *green* agent densities are $d_r(0) = 0.05$ and $d_g(0) = 0.2$, as shown in Fig. 4(a). In (**a**)–(**b**), $P_p = 0.1$. (**a**) Single realization at time $t = 60$. (**b**) Evolution of the average index (from $N = 50$ simulations) for the two species (*red* and *green*) and total population (*blue*). The *broken curves* are the corresponding I_{xcsr} values. In (**c**)–(**f**), $P_p = 0.01$. (**c**) Single realization at time $t = 60$. (**d**) Evolution of the average index (from $N = 50$ simulations) for the two species (*red* and *green*) and total population (*blue*). The *broken curves* are the corresponding I_{xcsr} values. (**e**) Long-time ($t = 600$) CA average column densities for the individual species (*red* and *green*) and total population (*blue*). The *broken black lines* (*top to bottom*) are the corresponding continuum solution, $C(x,t)$, $G(x,t)$ and $R(x,t)$, respectively. (**f**) Long-time evolution of the average index (from $N = 50$ simulations) for the two species (*red* and *green*) and total population (*blue*). The *broken curves* are the corresponding I_{xcsr} values

in Fig. 6(b). This slight deviation from the CSR state, for a small proliferation rate, is because the proliferation mechanism begins to (spatially) dominate again, as the domain approaches carrying capacity. However, it is interesting to note that the continuum equations for the individual species $R(x,t)$ and $G(x,t)$ (Binder and Landman 2009, (20) and (21)), and total population $C(x,t)$, (2), still accurately predict the long-time average column densities of the CA model, which is illustrated in Fig. 6(e). We found similar results to those shown in Figs. 6(e) and (f) for other initial conditions, where the agents were distributed non-uniformly throughout the domain.

When considering both the ENC agent proliferation and domain agent growth (linear) mechanism together, we find the individual species and total population indices are in general not at the CSR state (see Fig. 7). The growth mechanism essentially

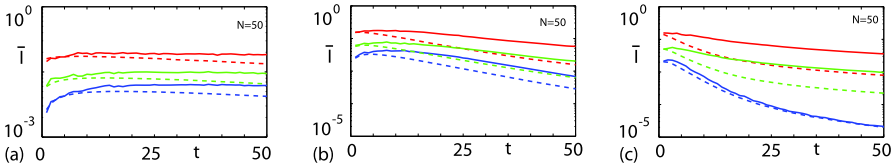

Fig. 7 Proliferation and domain growth (linear) mechanism, with $L(0) = 20$ and $\beta = 5$. The initial *red* and *green* agent densities are $d_r(0) = 0.25$ and $d_g(0) = 0.5$, as shown in Fig. 5(a). Evolution of the average indices (from $N = 50$ simulations, *solid curves*) with their $I_{x\text{csr}}$ values (*broken curves*). In (**a**)–(**c**), $P_p = 0.01$, $P_p = 0.1$ and $P_p = 0.5$, respectively

transports (see (2)—advection term) the segregated patches of ENC agents along the length of the growing domain. Although there is localized dispersion or spread (see (2)—local diffusion term) of the patches of ENC agents, there are areas of the domain void of ENC agents, which are also increasing in size. Only when the domain is fully occupied does the total population index attain the CSR state (see blue curves in Fig. 7(c)). A heuristic argument allows us to determine when the domain is fully occupied by ENC agents.

We consider the continuum model when the average column density is independent of x. We can then replace $C(x, t)$ in (2) by d to give an ordinary differential equation as

$$\dot{d}(t) = P_p d(1-d) - d\frac{\dot{L}}{L}\left(1 + \frac{1}{L+1}\right). \tag{11}$$

For linear domain growth (as in Fig. 7(c)), the dilution (last) term in (11) vanishes as $t \to \infty$ and, therefore, in this limit, $d \to 1$ and the CSR state eventuates (see Fig. 7(c), $t > 25$). We also confirmed this result for the index of the total populations shown in Figs. 7(a)–(b) (not shown here, since $t \leq 50$). In contrast, for exponential domain growth the dilution term does not vanish as $t \to \infty$ and, therefore, the domain is never fully occupied.

3.3 All Three Mechanisms

We now combine all three mechanisms, with linear domain growth. We first investigate a moderately high value of ENC agent proliferation relative to ENC agent motility, with the initial total density $d = 1$ but in three different proportions of 1:9, 3:7, and 1:1 for the two ENC agent species. Figures 8(a–c) show the distribution of the two species at $t = 30$, where the total ENC agent density is almost at carrying capacity. When the proportion is low, it is readily apparent that the red ENC agents are not at the CSR state. The patches of red ENC agents are similar to what is observed in the experiments of Figs. 1(c) and (d). When the two species are in the same proportion, one might conclude that they are fairly evenly distributed from Fig. 8(c), similar to those in Fig. 1(b). However, Figs. 8(d–f) tell a different story. When the spatial distributions are quantified using the index, we see that the individual species are never at the CSR state (except by definition at $t = 0$) for all three proportions—in particular they are (equally) far from the CSR state when they are in the same proportion (Fig. 8(f)). For the other two cases, the red agents are at a lower density, but they

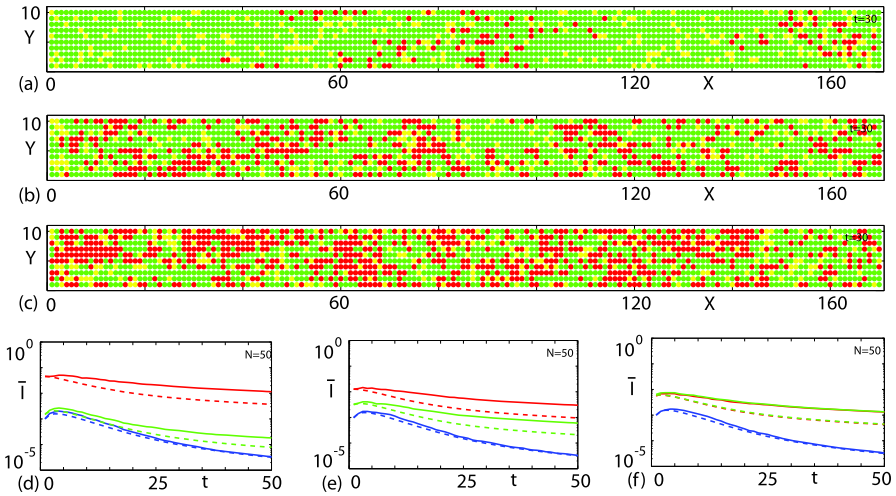

Fig. 8 Motility, proliferation, and domain growth (linear) mechanism, with $P_m = 1$, $P_p = 0.3$, $L(0) = 20$, and $\beta = 5$. (**a**)–(**c**) Typical simulations at time $t = 30$ where the initial dimensions of the domains were $X = 20$ and $Y = 10$ with evenly distributed densities $d_r(0) = 0.1$ and $d_g(0) = 0.9$, $d_r(0) = 0.3$ and $d_g(0) = 0.7$, $d_r(0) = d_g(0) = 0.5$, respectively. (**d**)–(**f**) Evolution of the average indices (from $N = 50$ simulations, *solid curves*) with their $I_{x\text{CSR}}$ values (*broken curves*). They correspond to the initial conditions of (**a**)–(**c**), respectively

are further from the CSR state than the more abundant species (green) (Figs. 8(d–e)), the graphs being on a log-scale. The total population deviates from the CSR state as time evolves, but near $t = 50$ it is close to the CSR state as the density is approaching carrying capacity.

We next investigate the three mechanisms when the initial total density is $d = 0.2$. In this case, there are only 20% as many agents as in Fig. 8, but the proportion of red to green ENC agents is the same as in Fig. 8 (1:9, 3:7 and 1:1 in columns 1–3, respectively). When the proliferation rate is the highest value (the same as in Fig. 8), (Figs. 9(a–c)), it takes more time than in Fig. 8 for the lattice to fill—this results in the total population taking longer to reach the CSR state. As expected, the individual species are far from CSR state. As the proliferation rate decreases in Figs. 9(d–f), it is still strong enough to demonstrate aggregation of same-species ENC agents but not sufficiently high enough that the lattice is at carrying capacity by $t = 50$. Therefore, the total and individual species are all far from the CSR state. However, if the proliferation rate is sufficiently low, all three populations remain close to the CSR state for all (moderate) time (Figs. 9(g–i)).

We find qualitatively similar results for exponential growth to those of Figs. 8 and 9(a–f), with the exception that the total ENC agent population is not at the CSR state. When the ratio of the ENC agent proliferation rate to the ENC agent motility rate is sufficiently low, the individual species and total population are at the CSR state for all time, as in Figs. 9(g–i).

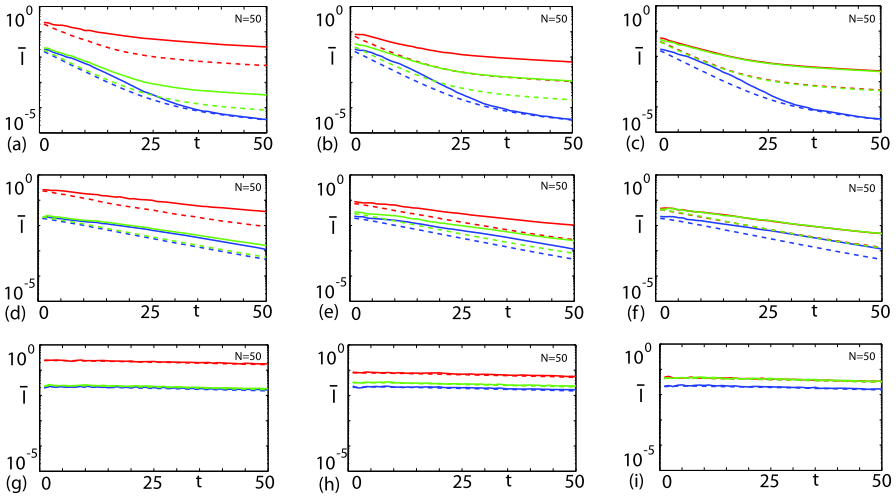

Fig. 9 Motility, proliferation, and domain growth (linear) mechanism, with $P_m = 1$, $L(0) = 20$ and $\beta = 5$. Evolution of the average indices (from $N = 50$ simulations, *solid curves*) with their I_{xcsr} values (*broken curves*). The initial densities are varied: Column 1 $d_r(0) = 0.02$ and $d_g(0) = 0.18$; Column 2 $d_r(0) = 0.06$ and $d_g(0) = 0.14$ and Column 3 $d_r(0) = d_g(0) = 0.1$. The number of agents is 20% of the number in Fig. 7. *The rows of the figure* are for decreasing values of the probability of proliferation. (**a**)–(**c**) $P_p = 0.3$. (**d**)–(**f**) $P_p = 0.1$. (**g**)–(**i**) $P_p = 0.01$

4 Discussion

The origin of the patchy distribution of GFP-labeled ENC cells in the avian embryonic intestine (Figs. 1(c) and (d)) is far from obvious since the total ENC population is relatively evenly distributed. The patches are highly diverse in their position along the gut, in the number of cells within each patch, and in the area occupied. Moreover, these patchy distributions contrast sharply with other distributions of GFP-labeled ENC cells that appear evenly distributed throughout most of the intestine (Fig. 1(b)). Intuitively, these patchy distributions of ENC cells depend on the percentage of the initial neural crest cell population that is labeled. We have confirmed this with our CA simulations and spatial-point data analysis (Fig. 8). The normalized spatial-variability (index) in low numbers of initially labeled ENC agents is several orders of magnitude larger than the total ENC population, which is relatively evenly distributed. However, our CA modeling along with the statistical analysis has shed-light on the spatial properties of the underlying total ENC agent distribution, which is likely to be mirrored qualitatively in the unlabeled and undetectable total ENC cell population.

By first examining each of the three main mechanisms (ENC proliferation and motility, and gut growth) in the migration process, and then combinations of the mechanisms together, we find that the ratio of ENC proliferation to motility is a key parameter producing vastly varying spatial distributions. Even moderate values of this ratio generate aggregations of ENC agents. We show that the total ENC agent population is at its most evenly distributed state, the CSR state, only when either this ratio is small or the domain is fully occupied—the latter only being applicable when the growth is linear.

The initial condition (evenly distributed ENC agents on the entire domain) used in our simulations may not be the same as in the experiments. In the experiments, there is no method for controlling the initial number and spatial distribution of the labeled cells. Therefore, the initial distribution of labeled cells is not necessarily evenly distributed, as in the simulations. However, an uneven distribution of labeled ENC agents (in the simulations) only increases the variability (number and size of patches) in the results. We are then just measuring this variability from an (initially) controlled evenly distributed state. Also, the gut tissue is not fully colonized at the start of the migration in the experiments, but at some later time there is complete colonization for a successful ENC cell migration. In some simulations (not presented here), we initially populated a region at the foregut end of our domain with ENC agents. When the ENC agent invasion had reached the anal end of the domain in the simulations, we sampled spatial-point data from the domain behind the invasion wavefront, where the ENC agent column density had achieved its preferred carrying capacity. We find similar results to those presented here.

Past modeling of the colonization of the ENS has demonstrated the importance of ENC cell proliferation in comparison with the motility (Simpson et al. 2007b; Zhang et al. 2010). Our analysis here strongly suggests that the appearance of labeled ENC patches may be caused by dominance of ENC proliferation to other mechanisms, reinforcing previous conclusions.

Acknowledgements This work was supported by an Australian National Health Medical Research Council grant and also by the Victorian Government's Operational Infrastructure Support Program. Kerry Landman is an ARC Professorial Fellow. We also thank Jon Chapman (University of Oxford) for his helpful suggestions and Craig Smith (Murdoch Children Research Institute) who provided the SoxE primary antibody.

Appendix: Experimental Methods

A.1 GFP Construct

The transposon mediated pT2K-CAGGS-GFP expression construct encoding EGFP, and the pCAGGS-T2TP expression construct encoding transposase has been described by Sato et al. (2007). These were prepared using a QIAfilter Plasmid Midi kit (12243; QIAGEN, Hilden, Germany), and resuspended in water to 3.6–4 μg/μl.

A.2 Preparation of Embryos

Fertile quail eggs (*Coturnix coturnix japonica*) were obtained from Lago Game (Melbourne, Australia) and incubated for 1.3 days (6–9 somite stage). Conventional techniques (Simkin et al. 2009) were used to prepare the embryos. Briefly, 1 ml of albumen was removed via syringe from quail eggs, and the embryos were exposed by opening a window in the shell, after which the albumen was returned. To visualize the embryo, sub-blastodermal injection of India ink (Pelikan No. 17 Black; Pol Equipment, Sydney) in PBS (1:4 dilution) was used. The vitelline membrane was moistened with a few drops of Tyrode's or Hank's Balanced Salt Solution then, using

a tungsten needle bent into a hook, a small tear was made in the vitelline membrane directly above the vagal injection site. Using a tungsten needle, a slit just large enough to insert the tip of a glass micropipette was made at the roof of the vagal level neural tube.

A.3 Injection of Construct

1 µl of pT2K-CAGGS-GFP and 1 µl of pCAGGS-T2TP were mixed together in a standing drop on a sterile 3 cm non-tissue culture dish. A trace of Fast Green dye (less than 0.5 µl) was added to allow for construct visibility. The standing drop was occasionally reconstituted with water to compensate for evaporation when the dish was open. Glass micropipettes (program 4, model P-87, flaming/brown micropipette puller, Sutter Instrument Co., USA) were used to micro-inject the construct into the neural tube lumen at vagal levels for neural tube and crest transfection.

A.4 Electroporation and Observation

For unilateral neural tube electroporation at vagal level in E1.3 embryos, parameters were three 10–12 V, 50 msec pulses at one second intervals using a BTX ECM 830 square-wave electroporator (Fisher Biotec, Melbourne, Australia). For bilateral electroporation, similar parameters were delivered to each side of the embryo. Electrodes were gold, with a length of 1 or 3 mm, and were positioned with a 3 mm separation on the vitelline membrane parallel to and on each side of the embryo. After electroporation, the eggs were sealed with adhesive tape and returned to the incubator. Embryos were monitored 12–24 h later by peeling back the tape and placing under a Leica MZ FLIII (Leica Microsystems, Switzerland) fluorescence stereomicroscope fitted with filters for GFP and Leica DC200 digital camera III system with Leica IM1000 software. Embryos with no GFP expression in the neural tube were discarded. Eggs were then resealed and further incubated for a total of 4 to 6 days post-electroporation. The embryos were then removed, washed in PBS, and the gastrointestinal tract was dissected out and fixed in 4% paraformaldehyde in PBS for 1 hr. Guts with GFP expression visible with the fluorescence stereomicroscope (post-electroporation 4 days, $N = 24$; 5 days, $N = 19$; 6 days, $N = 7$) were retained for further examination.

A.5 Immuno-Labeling and Microscopy

Specimens were blocked with 1% horse serum with 0.1% Triton X100 in PBS for 30 min. Specimens were then incubated overnight at 4°C sequentially in primary and secondary antibodies and other ligands prepared in block solution. Between treatments, the specimens were washed extensively in PBS. Specimens were mounted in Vectashield antifade reagent (Vector Laboratories, Inc., Burlingame, CA, USA) for microscopy. The primary antibodies, concentrations and sources used were: anti-SoxE rabbit IgG (1/5000, Dr. Craig Smith, MCRI), anti-GFP goat IgG (1/400, Rockland Immunochemicals, Gilbertsville, PA), anti-HuC/D mouse IgG (1/100, Molecular Probes/Invitrogen, Eugene, OR, USA). The respective secondary antibodies, concentrations and sources used were: anti-sheep/goat IgG, Alexa 488 conjugated

(1/400, Molecular Probes), anti-mouse Alexa 594 conjugated (1/2000, Molecular Probes), anti-rabbit IgG biotin conjugated (1/200, Jackson Immunoresearch, West Grove, PA, USA). Tertiary label was streptavidin, AMCA conjugated (1/100, Jackson). Specimens were analyzed under selective filters using an Olympus IX 70 microscope (Olympus Optical Co., Tokyo, Japan) with Image-Pro Plus software (Media Cybernetics, Silver Spring, MD, USA) and Leica CLSP confocal microscope. Specimens were stored in darkness at 4°C to reduce the degradation of the fluorescence signal.

References

Allan, I. J., & Newgreen, D. F. (1980). The origin and differentiation of enteric neurons of the intestine of the fowl embryo. *Am. J. Anat.*, *157*, 137–154.

Bhattacharyya, S., Kulesa, P. M., & Fraser, S. E. (2008). Vital labeling of embryonic cells using fluorescent dyes and proteins. *Methods Cell Biol.*, *87*, 187–210.

Binder, B. J., & Landman, K. A. (2009). Exclusion processes on a growing domain. *J. Theor. Biol.*, *259*, 541–551.

Binder, B. J., & Landman, K. A. (2011). Quantifying evenly distributed states in exclusion and non-exclusion processes. *Phys. Rev. E*, *83*, 041914.

Binder, B. J., Landman, K. A., Simpson, M. J., Mariani, M., & Newgreen, D. F. (2008). Modeling proliferative tissue growth: a general approach and an avian case study. *Phys. Rev. E*, *78*, 031912.

Diggle, P. J. (1983). *Statistical analysis of spatial point patterns*. London: Academic Press.

Hao, M. M., Anderson, R. B., & Young, H. M. (2009). Development of enteric neuron diversity. *J. Cell Mol. Med.*, *13*, 1193–1210.

Jones, S. W. (1991). The enhancement of mixing by chaotic advection. *Phys. Fluids A*, *3*, 1081.

Newgreen, D., & Young, H. M. (2002). Enteric nervous system: development and developmental disturbances-Part 1. *Pediatr. Dev. Pathol.*, *5*, 224–247.

Newgreen, D. F., Southwell, B., Hartley, L., & Allan, I. J. (1996). Migration of enteric neural crest cells in relation to growth of the gut in avian embryos. *Acta Anat.*, *157*, 105–115.

Phelps, J. H., & Tucker, C. L. (2006). Lagrangian particle calculations of distributive mixing: limitations and applications. *Chem. Eng. Sci.*, *61*, 6826–6836.

Sato, Y., Kasai, T., Nakagawa, S., Tanabe, K., Watanabe, T., Kawakami, K., & Takahashi, Y. (2007). Stable integration and conditional expression of electroporated transgenes in chicken embryos. *Dev. Biol.*, *305*, 616–624.

Simkin, J. E., McKeown, S. J., & Newgreen, D. F. (2009). Focal electroporation in ovo. *Dev. Dyn.*, *238*, 3152–3155.

Simpson, M. J., Merrifield, A., Landman, K. A., & Hughes, B. D. (2007a). Simulating invasion with cellular automata: connecting cell-scale and population-scale properties. *Phys. Rev. E*, *76*, 021918.

Simpson, M. J., Zhang, D. C., Mariani, M., Landman, K. A., & Newgreen, D. F. (2007b). Cell proliferation drives neural crest cell invasion of the intestine. *Dev. Biol.*, *302*, 553–568.

Simpson, M. J., Landman, K. A., & Hughes, B. D. (2010). Cell invasion with proliferation mechanisms motivated by time-lapse data. *Physica A*, *389*, 3779–3790.

Young, H. M., Turner, K. N., & Bergner, A. J. (2005). The location and phenotype of proliferating neural-crest-derived cells in the developing mouse gut. *Cell Tissue Res.*, *320*, 1–9.

Zhang, D., Brinas, I. M., Binder, B. J., Landman, K. A., & Newgreen, D. F. (2010). Neural crest regionalisation for enteric nervous system formation: implications for Hirschsprung's disease and stem cell therapy. *Dev. Biol.*, *339*, 280–294.